PNAS RESEARCH ARTICLE | ENGINEERING DEVELOPMENTAL BIOLOGY

Measurement of adhesion and traction of cells at high yield reveals an energetic ratchet operating during nephron condensation

Jiageng Liu[a,b], Louis S. Prahl[a,c], Aria Zheyuan Huang[a,b], and Alex J. Hughes[a,b,c,d,e,f,g,h,1]

Affiliations are included on p. 9.

Edited by David Weitz, Harvard University, Cambridge, MA; received March 5, 2024; accepted August 21, 2024

Developmental biology-inspired strategies for tissue-building have extraordinary promise for regenerative medicine, spurring interest in the relationship between cell biophysical properties and morphological transitions. However, mapping gene or protein expression data to cell biophysical properties to physical morphogenesis remains challenging with current techniques. Here, we present multiplexed adhesion and traction of cells at high yield (MATCHY). MATCHY advances the multiplexing and throughput capabilities of existing traction force and cell–cell adhesion assays using microfabrication and a semiautomated computation scheme with machine learning–driven cell segmentation. Both biophysical assays are coupled with serial downstream immunofluorescence to extract cell type/signaling state information. MATCHY is especially suited to complex primary tissue-, organoid-, or biopsy-derived cell mixtures since it does not rely on a priori knowledge of cell surface markers, cell sorting, or use of lineage-specific reporter animals. We first validate MATCHY on canine kidney epithelial cells engineered for rearranged during transfection (RET) tyrosine kinase expression and quantify a relationship between downstream signaling and cell traction. We then use MATCHY to create a biophysical atlas of mouse embryonic kidney primary cells and identify distinct biophysical states along the nephron differentiation trajectory. Our data complement expression-level knowledge of adhesion molecule changes that accompany nephron differentiation with quantitative biophysical information. These data reveal an "energetic ratchet" that accounts for spatial trends in nephron progenitor cell condensation as they differentiate into early nephron structures, which we validate through agent-based computational simulation. MATCHY offers semiautomated cell biophysical characterization at >10,000-cell throughput, an advance benefiting fundamental studies and new synthetic tissue strategies for regenerative medicine.

bioengineering | morphogenesis | cell sorting | kidney development

Significance

Cell biophysical properties drive tissue organization and are a target for guiding self-organization in tissue engineering. However, quantitative information on these properties is sparse. Classifying cellular identities and biophysical parameters at high throughput would accelerate progress. However, acquiring cell type-indexed information from primary tissue- or stem cell-derived cell suspensions is currently challenging. We address this through microfabrication, data processing, and modeling. We present multiplexed adhesion and traction of cells at high yield (MATCHY) for high-throughput measurements of cells dissociated from in vitro cultures or primary tissues, coupled to identity/state and signaling readouts. We apply MATCHY to cell biophysical transitions in mouse nephrogenesis, revealing an energetic ratchet occurring during nephron condensation. We anticipate diverse applications for MATCHY across morphogenesis and disease.

Cell collective mechanics are the proximate cause of tissue morphogenesis (1)—the tissue growth, shape change, and interfacial geometry between cell compartments that determine normal and diseased organ function (Fig. 1*A*). Interactions between cell tension, adhesion, proliferation, and migration sculpt many organs and feedback on cell behavior, for example, in heart tube looping, craniofacial development, and condensation of hair follicle, feather, gut villus, and limb bud/digit structures (2–8). The formation of blood-filtering nephron structures in the developing kidney is an archetypal example of the relationship between radical mechanical and morphological transitions (9, 10). Cap mesenchyme cells (the nephron progenitors) surround the tips of the developing ureteric bud epithelial tree (the future urinary collecting ducts), differentiating in response to Wnt (11, 12) and other biochemical cues from the ureteric bud and surrounding stroma (13–21). Nephron progenitors periodically condense into early nephrons by mesenchymal-to-epithelial transition (MET) as they differentiate, in parallel with a transition in cytoskeletal and adhesion molecule expression typical among other METs (10, 22–27). However, this "cell state/biochemical layer" of understanding has not yet been paired with a commensurate "biophysical layer" of cell mechanical changes that guide nephron self-organization. The lack of a complete mechanochemical picture of development remains a significant barrier to tissue construction by developmental mimicry, a nascent paradigm in tissue engineering for regenerative medicine (28).

One difficulty that hobbles the construction of biophysical-layer understanding across developmental systems is a lack of accessible tools for the mechanical characterization of cells and tissues. Techniques such as atomic force microscopy (29–31), micropipette aspiration (32–34), optical tweezers (35, 36), droplet deformation (37, 38), and traction-force

The authors declare no competing interest.

This article is a PNAS Direct Submission.

[1]To whom correspondence may be addressed. Email: ajhughes@seas.upenn.edu.

This article contains supporting information online at https://www.pnas.org/lookup/suppl/doi:10.1073/pnas.2404586121/-/DCSupplemental.

Published September 18, 2024.

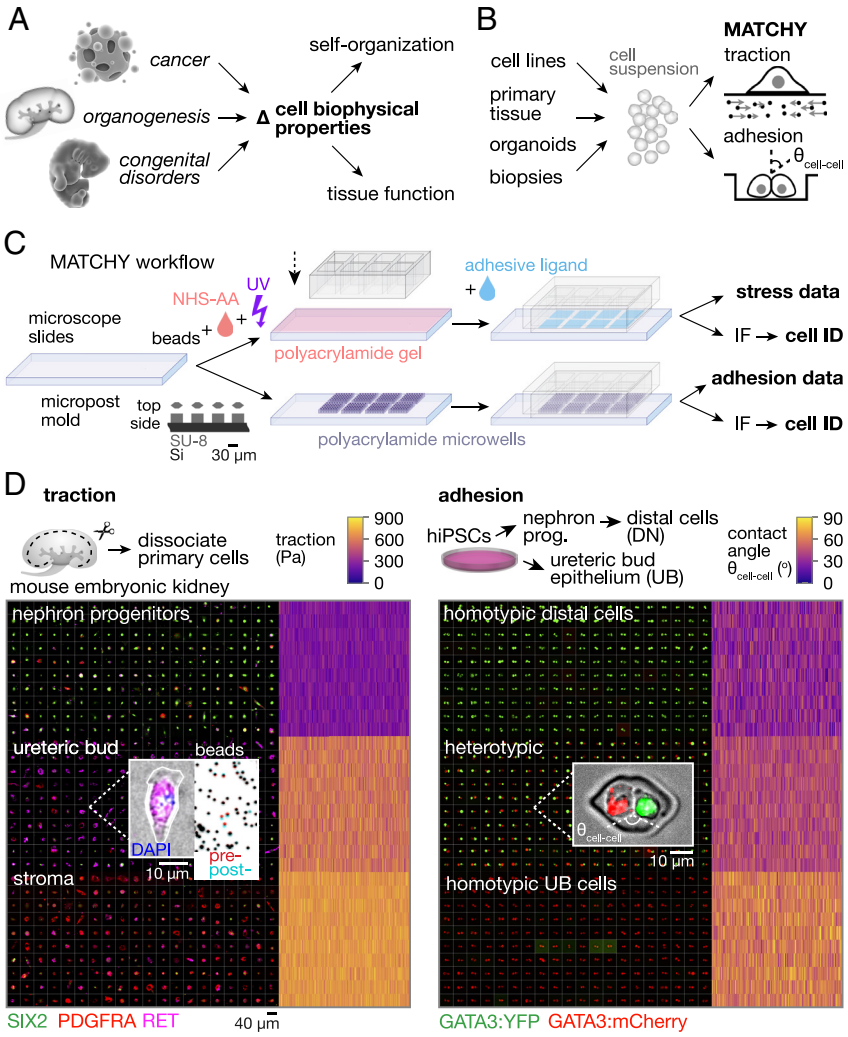

Fig. 1. MATCHY quantifies biophysical properties of cells in compositionally complex mixtures and associates them with cell type/signaling state at high throughput. (*A*) Schematic of biophysical contributions to tissue organization and function in development and disease. (*B*) Schematic of cell suspension sources for MATCHY cell traction and adhesion assays. (*C*) Schematic of microfabrication workflows for MATCHY traction and adhesion assays. (*D*) Example high-throughput traction and adhesion data for dissociated primary E17 mouse embryonic kidney cells and iPSC-derived kidney cell lineages, respectively. Traction data are summarized as a mosaic IF image (*Left*) of a subset of 200 cells per type category, along with a heatmap showing traction stress for 4,000 cells per category. *Inset*, example cell postfixation and IF staining, alongside fluorescent image of beads in the same area of substrate, as a projection of pre- and postfixation states. Contact angle data are summarized similarly (*Right*) for a subset of 200 doublets of GATA3 reporter iPSC-derived kidney cell lineages per type category out of 2,000 doublets per category. "Homotypic" refers to a contact angle measurement between two cells of the same type, while "heterotypic" refers to that between dissimilar cell types. *Inset*, example fluorescence micrograph of a cell doublet and microwell boundary, indicating one contact angle measurement.

microscopy (TFM) (39, 40) have yielded advances here (41). However, each of these techniques suffers from low throughput, high technical complexity, or both. In parallel, researchers have inferred drivers of self-organization during morphogenesis from genetic model studies, primary cell self-organization assays, and cytoskeletal/adhesion expression profiling (34, 41–44). For example in nephron-forming niches, knockout of tension and adhesion regulators including nonmuscle myosin II (Myh9/10) and integrin α8β1 (ITGA8) alter niche and early nephron organization, affecting nephrogenesis rate (45, 46). Cells dissociated from embryonic kidneys spontaneously recover some aspects of native spatial structure, at least at short spatial length scales. For example, ureteric bud aggregates (22) surrounded by SIX2+ nephron progenitors are capable of rudimentary branching (47) and some connectivity with distal domains of nearby reforming nephrons (48, 49). Researchers have made significant progress in defining a "cadherin code" that distinguishes anatomical compartments, namely differential expression of cadherins between naive nephron progenitors (*Cdh2*, *4*, *6*) and those undergoing MET to renal vesicles and later stages associated with nephron segmentation (*Cdh1, 2, 3, 4, 6, 11, 16*) (22, 23, 25, 50, 51). However, cadherin expression alone is not necessarily predictive of self-organization outcomes (52). Though differential adhesion/interfacial tension has been raised as a compelling theory explaining niche and (more specifically) nephron self-organization (10, 22, 50, 52–55), it remains to be tested with direct biophysical measurements.

Here, we present multiplexed adhesion and traction of cells at high yield (MATCHY), which enables TFM and cell doublet adhesion assays to be integrated with immunofluorescence (IF)-based cell type and state measurement (Fig. 1 *B–D*). MATCHY is powered by a computational pipeline designed for high-throughput and multiplexed measurements. We apply MATCHY to associate nephron progenitor lineages with biophysical states during mouse nephron development. We first validate MATCHY on a well-studied Madin-Darby canine kidney (MDCK) cell line engineered to express the receptor tyrosine kinase RET (56). RET functions through a ligand–receptor interaction with glial cell-derived neurotrophic factor (GDNF) to activate extracellular signal-related kinase (ERK) and other downstream signals to drive branching morphogenesis (57–60). ERK signaling, in turn, stimulates cell

traction forces across epithelial tissue layers (61). We show that cell traction forces can be measured upon cell fixation rather than lysis, enabling downstream analyses such as IF for phospho-ERK (active ERK) using semiautomated data analysis. We next apply MATCHY to measure traction forces produced by single cells in heterogeneous primary cell populations dissociated from the mouse embryonic kidney "nephrogenic zone." We leverage the ability of our pipeline to retrospectively link cell traction and identity in these heterogeneous cell mixtures. We then repeat a similar analysis for cell doublet adhesion assays in microwell arrays. These measurements together serve as a biophysical atlas of nephron progenitor lineage commitment, showing progressively increasing cell traction and homotypic adhesion along the nephron condensation "trajectory." Heterotypic adhesion data reveal an energetic benefit that would tend to drive cells toward physical segregation from the nephrogenic niche, as observed in vivo. Specifically, we find that the heterotypic adhesion of a given nephron lineage cell type with its most closely related differentiation state is higher than its homotypic adhesion (with cells of the same state), which we refer to as an "energetic ratchet." We show that biophysical data alone are partially sufficient to account for nephrogenic niche-like and early nephron structure formation using agent-based modeling and primary cell spheroid self-organization assays.

Together, these data establish MATCHY as a flexible tool for mechanical analysis of cell mixtures and provide a biophysical basis for nephron formation by MET. By linking such data to organizational outcomes, we establish an engineering blueprint for synthetic nephrogenesis through cell engineering or other methods requiring initial or boundary biophysical conditions. Such data will inform future efforts to generate uniform, compact arrays of functional nephrons for kidney replacement duty. MATCHY is designed for application across a variety of cell systems, enabling biophysical characterization of organization across diverse applications in development, disease, and engineered tissues.

Results

We designed MATCHY to correlate cell biophysical information with cell identities/states. This is achieved through simultaneous, multiplexed measurement of cell traction forces/cell–cell adhesion and protein biomarker expression. For the traction arm of MATCHY, we fabricate polyacrylamide gel sheets with validated mechanical properties (62, 63) bearing fluorescent microparticles as fiducial markers on standard microscopy slide substrates (Fig. 1*C*). Cell-adhesive ligands (specifically Matrigel in this study) are then covalently bound to the gel via an *N*-hydroxysuccinimide (NHS) ester-functionalized acrylic acid comonomer (63) after assembling substrates into a modular culture well system. Cells adhere and develop traction forces that can be visualized as a strain field through deflection of the fluorescent microparticles. Traditionally this is done by comparing bead positions local to cells in the stressed state to those after cell traction has been ablated via cell detachment/lysis (39). For the cell–cell adhesion arm of MATCHY, we adapted a microwell-based approach to create highly parallelized arrays of cell doublets (44). We polymerized a 30-μm-thick sheet of nonadhesive polyacrylamide around arrays of 20 × 40 μm microposts fabricated through photolithography. Once demolded, these arrays enriched for the capture of cell doublets from cell suspensions settled into them by gravity (64). Cells then form contacts upon incubation that report on adhesion energy through their contact angle (41, 44, 65).

For the traction arm, we reasoned that IF staining could be integrated with traditional traction force microscopy by replacing cell lysis with fixation. Cell fixation still relaxes cell traction stress (66) while permanently adhering cells to the polyacrylamide substrate, enabling a serial IF assay. Indeed, reading out cell traction by fixation successfully recovered 72% of total traction magnitude measured by traditional cell lysis in a human-induced pluripotent stem cell (iPSC) population (*SI Appendix*, Fig. S1*A*). A more detailed study on a single-cell basis verified that this ratio was independent of cell type and stress magnitude over a ~0 to 1,000 Pa range in cell traction by fixation (*SI Appendix*, Fig. S1*B*). Fixation was also sufficient to retain >70% of cells on the substrate throughout subsequent IF staining steps for MDCKs. This enabled the quantitation of cell identity markers for subsequent cell type classification in series with the traction assay. For the cell–cell adhesion arm, we similarly found that the polyacrylamide microwell substrate was compatible with automated imaging of endogenous fluorescence of reporter iPSCs and of markers stained by IF in situ. >50% of cell doublets were retained in wells throughout the IF staining steps regardless of cell type, enabling subsequent cell type classification in series with the cell–cell adhesion assay as in the traction arm.

We next created semiautomated experimental and image analysis processes for both arms of MATCHY. For the traction arm, we instituted high-throughput, "one-button" image acquisition and preprocessing, multiplexed cell detection, traction force microscopy by Fourier transform traction cytometry (FTTC) (67), and cell type classification based on IF marker expression (*SI Appendix*, Fig. S2). For the cell–cell adhesion arm, we performed similar automated image acquisition knowing the nominal microwell array dimensions, image filtering to enrich for cell doublets in proper contact, contact angle annotation, and cell type classification. This process enables high-throughput characterization of, e.g., primary tissue- and iPSC-derived cell populations (Fig. 1*D*) (68).

Of the two biophysical measurements comprising MATCHY, the traction arm required modification from standard practice to integrate IF, whereas our primary contribution to the adhesion arm is a higher-throughput implementation. For deeper validation of the traction arm, we turned to an MDCK cell line overexpressing the human RET9 receptor (MDCK-RET) (56) (*SI Appendix*, Fig. S3*A*). These cells model RET's crucial role in branching morphogenesis of the developing kidney ureteric bud (59, 60) (Fig. 2*A*). MDCK-RET cells change their adhesive properties and scatter in response to GDNF (56). Cells activate pERK downstream of GDNF-RET and MEK signaling, which also involves a coreceptor GDNF-receptor alpha 1 (GFRA1) (57, 69). ERK phosphorylation (pERK) stimulates contractile pulses within MDCK cell layers by activating the Rho/ROCK pathway (61). A similar action of RET through Rho has been observed in other cell types (70, 71). In 2D culture, we verified that the addition of GDNF + GFRA1 induced MDCK-RET cell scattering, while untreated cells maintained intact colonies (Fig. 2*B*). However, a quantitative relationship between GDNF-RET signaling and traction force has not been determined. We quantified the traction force of MDCK-RET cells treated with GDNF + GFRA1 relative to negative controls consisting of untreated cells, those treated with GFRA1 only, those treated with GDNF + GFRA1 + the MEK inhibitor trametinib (MEKi), or those treated with the Rho-associated protein kinase (ROCK) inhibitor Y-27632 (ROCKi) or myosin II ATPase inhibitor blebbistatin (Fig. 2 *C*–*E*). GDNF + GFRA1 increased traction stresses by 1.6-fold, while cells treated with GFRA1 alone showed no increase (Fig. 2*D*). MEKi ablated the traction increase associated with GDNF + GFRA1 treatment. ROCKi and blebbistatin treatments also significantly ablated traction stresses relative to untreated cells. Leveraging our ability to simultaneously measure

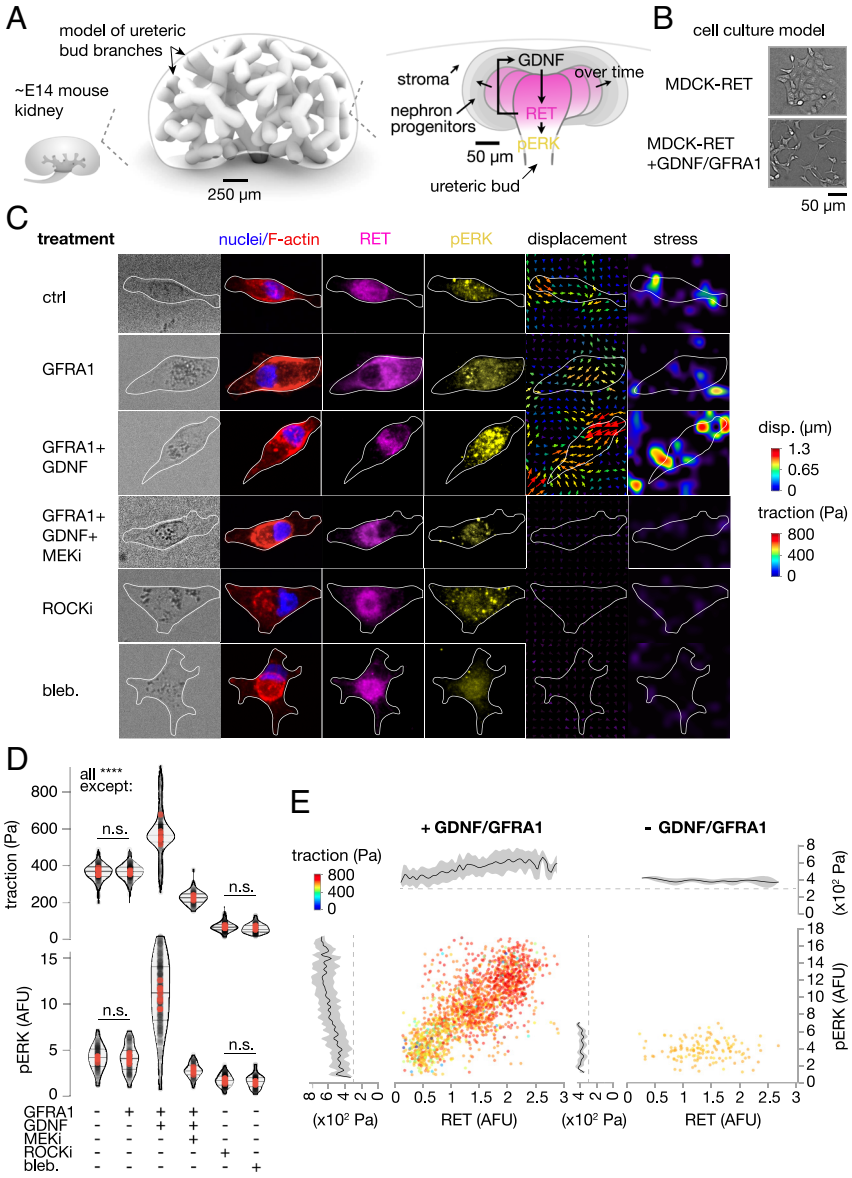

Fig. 2. MATCHY captures cell traction effects of GDNF-RET signaling at high throughput. (*A*) Model schematic of ureteric bud tubule branching in the embryonic kidney. *Right*, detail of nephrogenic niche anatomy at ureteric bud tips and the role of RET in MAPK activation via ERK. (*B*) Phase contrast micrographs of RET-expressing MDCK cell line as a reductionist model, with and without 12 h activation using 50 ng/mL GDNF and 100 ng/mL coreceptor GFRA1. (*C*) Montage of phase and immunofluorescence micrographs and traction force microscopy output (displacement and stress fields) for representative MDCK-RET cells after the indicated treatments on adhesive polyacrylamide substrate. (*D*) Violin plots of traction force distribution for indicated treatments showing means and quartiles (gray lines, n = 8 replicate wells per condition. Red points are means of replicates. Total cell numbers were 138, 113, 178, 136, 255, and 134 cells, respectively. MEKi, trametinib; ROCKi, Y-27632; bleb., blebbistatin). One-way ANOVA, Tukey's test, ****P < 0.0001. (*E*) Plots of RET expression and pERK intensity by immunofluorescence upon GDNF/GFRA1 activation vs. untreated control (>1,700 cells combined across n = 8 replicate wells). Traction stress is represented by point color and by running average plots (window size of 25 cells).

RET marker expression and pERK level in the same cells, we noted a positive correlation between the two in the cell population for a fixed GDNF + GFRA1 stimulation (Fig. 2*E*). We further found that pERK is not activated by GDNF + GFRA1 in MDCK-RET kinase-mutant cells, verifying that GDNF acts through RET in these cells (*SI Appendix*, Fig. S3*B*). Traction stresses monotonically increased with RET expression in the presence of GDNF + GFRA1 and indicated a possible switch-like increase in cell traction at intermediate expression. In untreated controls, there was no correlation between RET level and ERK phosphorylation or cell traction. These data indicate successful implementation of traction force microscopy integrated with multiplexed detection of protein markers of cell identity and state by immunofluorescence.

Having validated MATCHY's TFM integrated with IF, we sought to create a biophysical atlas of the nephron-forming niche from primary mouse embryonic kidney cells (Fig. 3). These niches are defined by "caps" of mesenchyme (nephron progenitor cells) at the tips of the branching ureteric bud (72, 73) (Fig. 3*A*). Nephron progenitors proliferate in the niche and differentiate into early nephron cells that periodically condense by mesenchymal-to-epithelial transition into pretubular aggregates (PTAs) (55, 72–75). Such morphological transitions are often triggered by cell rearrangement caused by changes in cell cortical tension and cell–cell adhesion, a process partially explained by models such as the differential adhesion/differential interfacial tension hypothesis (52–54, 76, 77). Although nephron progenitors express a changing cell adhesion molecule profile as they transition along their differentiation

trajectory (10, 22, 24, 25, 75, 78–81), the downstream effect of this on cell biophysical properties has not been quantified. We first verified the molecular basis of nephron MET by analyzing existing mouse kidney scRNA-seq data published by Combes et al. (82). Gene set enrichment analysis of a precurated list of sets related to cell tension and adhesion revealed significant enrichment for all of them in cells from the PTA and renal vesicle clusters vs. those from the nephron progenitor and "primed" nephron progenitor clusters (Fig. 3*B*). Feature plots confirmed differential expression of cadherins *Cdh1, 2, 3, 4, 6*, and *11* over the nephron differentiation trajectory; each being previously identified as relevant to nephron MET and further development (22, 23, 25, 50, 51).

We next sought to quantify how these molecular-level changes relate to cell biophysical properties among differentiating nephron progenitors. Mapping the traction stresses of closely related cell lineages along a differentiation trajectory by traditional means requires them to be separately sorted and assayed. This is challenging or impossible for rare cell types or those having poorly characterized surface marker profiles. Alternatively, lineage-specific reporter mice can be produced to mark cell types of interest before sorting by endogenous fluorescence (83). However, this adds significant complexity. We instead recovered "nephrogenic zone" (surface/cortical layer) cells from E17 mouse embryonic kidneys by brief dissociation according to an established protocol (13, 68) and relied on post hoc assignment of cell identity after fixation and immunofluorescence for intracellular markers. This cell mixture is enriched for stromal, nephron progenitor, and early nephron lineages. Less than 10% of the recovered cells are mature nephron, ureteric bud, endothelial, or immune cells (13). We performed multiplexed traction force measurements and read out predicted cell identity using thresholds for canonical protein marker expression (Fig. 3*C*, nephron progenitor cells, NPC: CITED1+ SIX2+; primed NPC, PN: SIX2+; pretubular aggregate, PTA: SIX2 medium LHX1+; renal vesicle, RV: SIX2 low LHX1+ JAG1+; "beyond renal vesicle," BRV: LHX1 medium JAG1+) (84, 85). We then used t-SNE to reduce dimensionality and cluster distinct cell populations (Fig. 3*D*). Overlaying traction data onto these clusters showed a progressive increase along the differentiation trajectory from NPC to BRV. This predicts that MET is associated with an increase in cell contractility, which may be necessary for cell compaction from the niche into PTAs. Indeed, appropriate lumenization of PTAs during their transition to RVs requires nonmuscle myosin IIA (*Myh9*) and IIB (*Myh10*) expression, suggesting that cell contractility is required for the completion of MET (45). Our data indicate that cells exert higher traction stresses as they progress along the nephron differentiation trajectory.

We moved on to complement the finding of MET-associated increase in single-cell traction with data from the cell–cell adhesion arm of MATCHY. We read-out cell adhesion information via contact angle of cells in doublets incubated for 3 h, again inferring cell identities post hoc using immunofluorescence (*Methods*). Similar to our traction data, we measured a monotonically increasing homotypic adhesion along the nephron progenitor differentiation trajectory (Fig. 3*E*). The heterotypic adhesion for a given cell lineage tended to be higher with closely related daughter lineages compared to the homotypic adhesion for that lineage, for example, NPC–PN > NPC–NPC, PN–PTA > PN–PN, PTA–RV > PTA–PTA, and RV–BRV > RV–RV. This structure of increasing heterotypic adhesion to homotypic adhesion creates an "energetic ratchet" that may favor physical segregation and transit of cells through the morphological transition to renal vesicles and S-shaped bodies. Moreover, cell–cell adhesion appears to reach a maximum at around the RV stage, while traction continues to increase through the BRV stage. This ordering may be necessary to establish sufficient cell–cell adhesion to permit the radical shape change occurring in the nephron upon S-shaped body formation (9, 10, 86). These data indicate a substantial increase in cell–cell adhesion and traction along the differentiation trajectory that may drive structural transition in the developing nephron (Fig. 3*F*).

We next wondered whether biophysical modeling of our traction and adhesion data from primary mouse kidney cells would predict self-organization of the niche and early nephrons (Fig. 4*A*). Similar models have successfully predicted self-organization of other multicellular structures such as mammary acini (44) and early embryos (41). Previous models for embryonic kidney cell self-organization have partially predicted the effects of repulsion/attraction within and between the cap mesenchyme and the ureteric bud on bud/niche organization. However, these did not quantitatively measure cell biophysical properties or attempt to explain self-organization of nephron lineage cells during early nephrogenesis (22, 27, 87, 88). To address this question, we adapted a cellular Potts (agent-based) model for early embryo self-organization (41), drawing cell–cell adhesion and cortical tension parameters from our quantitative biophysical atlas distributions in Fig. 3 *D–F* (*Methods*). We paired the model with a self-organization assay consisting of spheroid cultures of the same primary cells (13) (Fig. 4*B*). In the model, we neglected possible contributions of ongoing cell differentiation and proliferation to reduce the number of parameters and simplify interpretation of outcomes. We hypothesized that the measured biophysical parameters from our experiments on dissociated primary nephrogenic zone cells may be sufficient to explain nephron condensation, location in the niche, and/or proximal–distal polarization (i.e., spatial ordering of cells along the differentiation trajectory during segment patterning, Fig. 4*A*). We reasoned that the model would enable testing these hypotheses.

Previous work has noted intimate interactions between cap mesenchyme (nephron progenitor) cells and the ureteric bud mediated by adhesion molecules such as ITGA8 (14, 82, 89). However, we did not recover ureteric bud cells and measure their traction or adhesion properties. Instead we assumed that their homotypic adhesion and heterotypic adhesion with nephron progenitors were arbitrarily high [since ureteric bud cells form core–shell structures with nephron progenitors in reaggregation assays (22, 47)]. We also assumed that the heterotypic adhesion between ureteric bud cells and more differentiated nephron lineages was negligible (since these never mix in vivo). Using cell–cell adhesion and traction force parameters drawn from our biophysical atlas in the simulation led to spontaneous clustering and agent cell organization given an initial cell composition similar to that in the mouse nephrogenic niche (Fig. 4 *C* and *D* and Movie S1*A*). We used an initial condition in which differentiated agent cells were initially randomly distributed, simplifying the more nuanced geometry of cell locations in the niche (84, 85, 90). Nevertheless, differentiated agents condensed and formed several qualitative morphologies roughly reminiscent of early polarized nephrons at the renal vesicle and S-shaped body stages (Fig. 4 *C* and *E*). Mimicking the condensation effect, LHX1+ JAG1+ early nephron cells formed clusters within our primary cell spheroids after 12 h culture (Fig. 4 *F* and *G*). In the model, both average cluster size and frequency of polarization phenotypes were significantly smaller when parameters were "scrambled" to undermine the energetic ratchet by randomly selecting values from the measured cell type distributions, though the total area fraction of clusters was unaffected (Fig. 4 *D* and *E*). We reasoned that a similar effect could be mimicked in the primary cell spheroids using published specific blocking antibodies to cadherins expressed in the early nephron (91–94). Indeed, average cluster size was significantly decreased in the presence of blocking antibodies for CDH1 (expressed in RV, BRV), CDH2 (NPC, PN, PTA), or CDH11

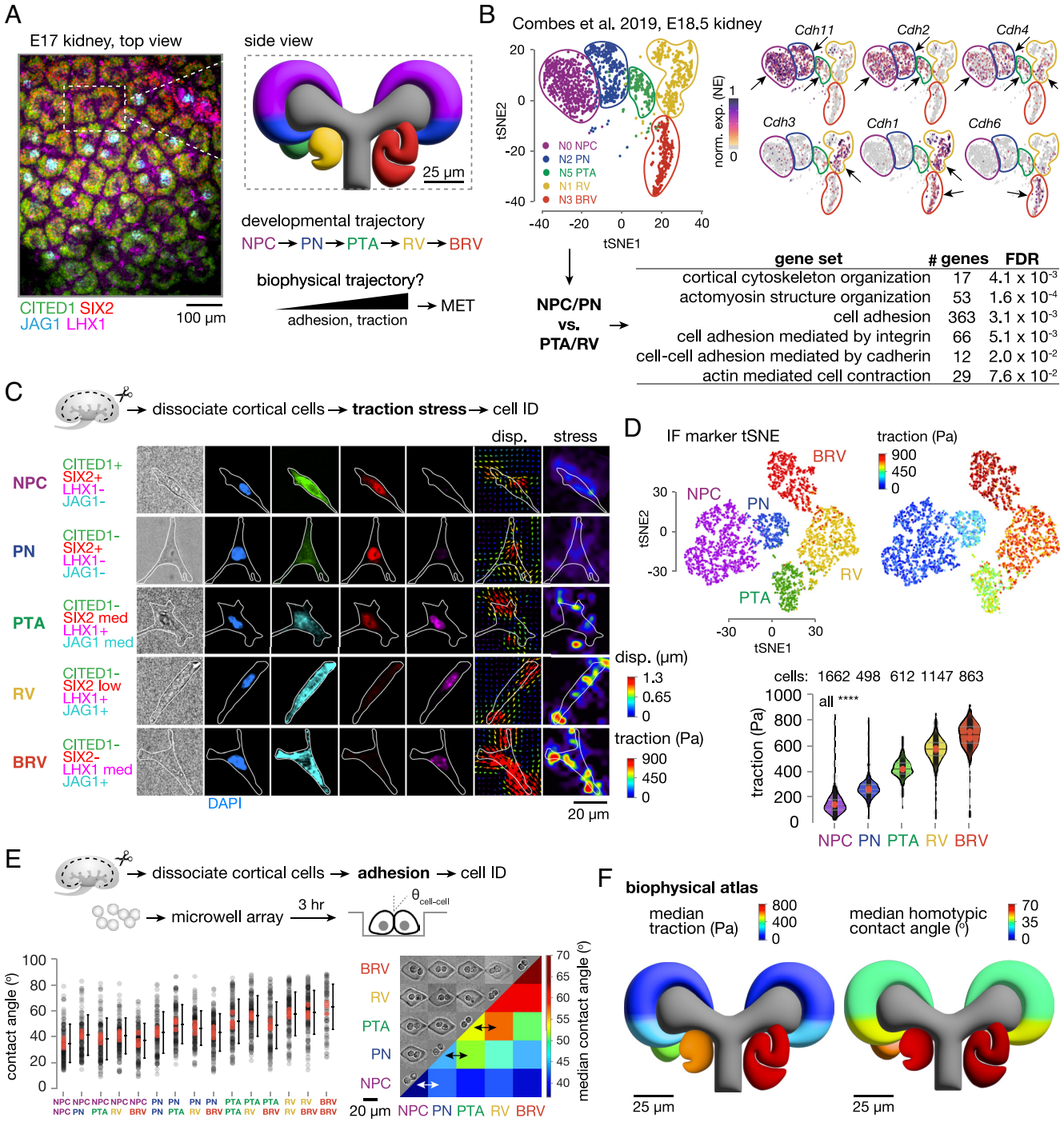

Fig. 3. A biophysical atlas of primary mouse nephrogenic niche cells reveals an energetic ratchet accompanying nephron progenitor differentiation. (*A*) *Left*, Whole-mount confocal immunofluorescence micrograph of E17 kidney cortical surface showing CITED1+ SIX2+ nephron progenitor niche compartments and LHX1, JAG1 differentiation markers. *Right*, schematic of niche anatomy and stages of nephron progenitor differentiation. NPC, nephron progenitor cell; PN, primed nephron progenitor; PTA, pretubular aggregate; RV, renal vesicle; BRV, beyond renal vesicle (comma-shaped body, S–shaped body, etc.). (*B*) *Top*, tSNE plot of cell clusters and feature plots of cadherin expression over the nephron differentiation trajectory from scRNA-seq data published in Combes et al. (82). Arrows indicate clusters having appreciable marker expression. *Bottom*, gene set enrichment analysis results for the listed sets, comparing NPC/PN stages to PTA/RV stages. (*C*) Montage of phase and immunofluorescence micrographs and traction force microscopy output (displacement, disp., and stress fields) for primary mouse E17 embryonic kidney nephrogenic zone cells representative of each cell type along the differentiation trajectory. (*D*) *Top*, t-SNE dimensionality reduction plots based on expression of the markers in (*C*) showing annotation of clusters by cell type (*Left*) and by traction force (*Right*). *Bottom*, Violin plots of traction force by cell type showing means and quartiles (gray lines, $n = 8$ replicate wells; red points are means of replicates). One-way ANOVA, Tukey's test, ****$P < 0.0001$. (*E*) Plot of cell–cell contact angle between the indicated homotypic and heterotypic pairs (mean ± SD, $n > 100$ pairs per comparison), and heat-map matrix of median contact angles. Arrows highlight the relationship between homotypic contact angle for a given cell type and that for its heterotypic contact with the most closely related cell type along the differentiation trajectory. (*F*) Biophysical atlas showing median traction and homotypic adhesion data mapped as colors onto the niche schematic.

(NPC, PN, PTA), though again the total area fraction of clusters was unaffected (22, 23, 50, 51, 82, 95) (Figs. 3*B* and 4 *F* and *G*). These data conflict with findings that genetic knockout of individual cadherins does not significantly undermine mouse nephron MET in CHIR-induced primary nephron progenitor cell cultures (specifically *Cdh2, 3, 4,* or *11*) or mouse models

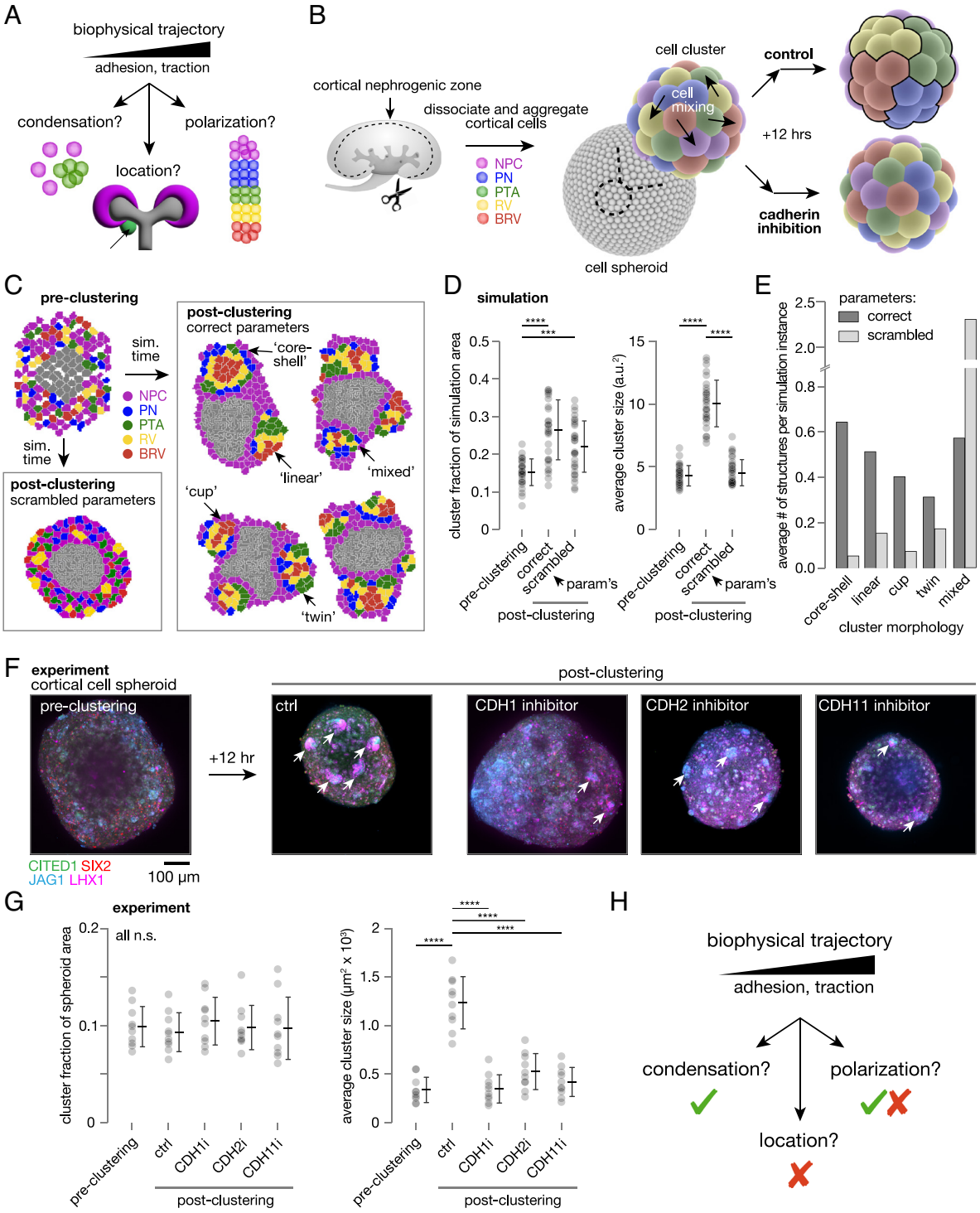

Fig. 4. An energetic ratchet in cell contractility and adhesion properties is sufficient to explain early nephron condensation and partially sufficient to explain subsequent polarization. (*A*) Schematic of nephron formation properties potentially affected by an energetic ratchet in cell–cell adhesion and tension during nephron progenitor commitment. (*B*) Schematic of hypothesis for dissociated mouse embryonic kidney cell self-organization driven by cell biophysical properties. NPC, nephron progenitor cell; PN, primed nephron progenitor; PTA, pretubular aggregate; RV, renal vesicle; BRV, beyond renal vesicle (comma-shaped body, S-shaped body, etc.). (*C*) Agent-based simulations of nephrogenic niche self-organization. *Top Left*, Example simulation initial condition with ureteric bud cells clustered together and other nephron lineage cells randomly arranged around it. *Bottom Left*, example "scrambled" parameter simulation with biophysical properties of nephron lineage cells randomly chosen from all traction and adhesion distributions. *Right*, example "correct" parameter simulations with biophysical properties of nephron lineage cells randomly chosen from the traction and adhesion distributions corresponding to their correct cell lineages. Condensed cell clusters are qualitatively annotated according to the indicated morphology types: "core–shell" (annular distribution of cell types along the differentiation trajectory), "linear" (linear distribution), "mixed" (no apparent order), "cup" (combining features of core–shell and linear), or "twin" (clusters with two linear axes fused with each other). (*D*) Plots of fraction of simulated nephrogenic niche occupied by clusters and average individual cluster size (area) at simulation start ("preclustering"), and end ("postclustering") for correct and scrambled parameter cases (points are simulation instances, mean ± SD, n > 30 simulations per condition). (*E*) Plot of representation of qualitative cell cluster sorting states in the model. (*F*) Immunofluorescence micrographs of primary E17 nephrogenic zone cell spheroids immediately after aggregation (*Left*), and after 12 h incubation in control media (ctrl) or in the presence of blocking antibodies for the indicated cadherins (*Right*). Arrows indicate condensed cell clusters. (*G*) Plots of fraction of spheroid area occupied by clusters, and average individual cluster size (area) at experiment start ("preclustering"), and end ("postclustering"), for spheroids cultured without ("ctrl") or with cadherin blocking antibody (points are spheroids, mean ± SD, n > 10 spheroids per condition). "CDH1i" = blocking antibody for CDH1, etc. (*H*) Schematic summary of biophysical prediction of nephron formation properties. Statistics in (*D*) and (*G*) are one-way ANOVA, Tukey's test, ***$P < 0.001$, ****$P < 0.0001$.

(*Cdh4*$^{-/-}$, *Cdh6*$^{-/-}$) (24, 50, 51). However, knockout of *Cdh6* (and potentially of *Cdh4*) does delay nephron epithelialization (24, 51). Furthermore, kidney explant culture magnifies the loss of MET for *Cdh4*$^{-/-}$ kidneys and when a blocking antibody for CDH6 is used in wild-type kidneys (23, 51). This indicates a lower robustness and/or slower kinetics of nephron condensation upon single cadherin perturbation that reveals itself in our spheroid assay for condensation of already differentiated rather than induced cells, as it does in explant culture. Overall, the primary cell and modeling data indicate that an energetic ratchet in nephron lineage cell biophysical properties is sufficient to explain early nephron condensation and some of the spatial organization of early mouse nephrons (Fig. 4*H*). Further robustness may be achieved in vivo through additional factors provided by the ureteric bud and surrounding stromal cells that are not currently captured by the model (19, 84, 96–98).

Discussion

Gene expression and signaling pathways operate through single-cell and supracellular biophysical properties to determine tissue structure (99). A quantitative understanding of biophysical changes along differentiation trajectories is therefore necessary to guide tissue organization in engineered, developing, and diseased tissues alike. Cell–cell heterogeneity necessitates high-throughput measurements to capture the full distribution of biophysical changes within and between multiple cell states. Here, we address these needs in MATCHY via microfabrication, serial integration of biophysical and molecular characterization assays, and machine learning automation. We achieve quantitation of adhesion and traction of >10,000 cells across >8 independent experimental conditions in the same experiment, all within 12 h of tissue dissociation. The MATCHY approach is adaptable to any tissue type amenable to single-cell dissociation. We chose kidney development as a case study due to the complexity of cell dynamics, decision-making, and self-organization within its nephrogenic niches. We first validated MATCHY performance for GDNF-RET tyrosine kinase signaling in a cell line model of its effects on ureteric bud branching morphogenesis. This revealed a correlation between MAPK signaling activation and downstream cell traction that scales with RET receptor expression. We then explored the multiplexing capability of MATCHY for primary cell suspensions prepared from mouse embryonic kidneys, finding monotonic increases in both cell traction and adhesion along the nephron differentiation trajectory that complement previous characterization of an expression-level adhesive switch program associated with MET. The adhesion data reveal an "energetic ratchet" among differentiating cell types where the heterotypic adhesion of a given cell type with its most closely related differentiation state is higher than its homotypic adhesion. This would tend to spatially recruit differentiating cells into progressively more mature tissue compartments, potentially explaining physical segregation of newly formed nephrons from the niche. To explore this, we performed agent-based modeling, which predicted condensation of early nephrons in the nephron progenitor niche using parameters sampled from cell experiments. The model also partially predicted spatial sorting of differentiation states in an analogous fashion to that occurring during polarization of the nephron in vivo. Together these data provide a biophysical atlas of nephrogenesis—an important roadmap for tissue engineering efforts to reconstitute nephrogenesis in iPSC-derived kidney organoids for regenerative medicine applications.

Our contributions here leave several areas for future study and consideration. First, we did not consider traction or adhesion properties of ureteric bud or stromal cells. These compartments form important niche boundary interfaces that likely contribute to nephron progenitor sorting dynamics. For example, the ureteric bud makes adhesive interactions with nephron progenitors through a range of cell–cell and cell–matrix ligand–receptor pairs, notably ITGA8–nephronectin, which is required for proper niche organization (46, 82, 89). Similarly, the underlying cause of new nephron positioning at the curved "armpits" of branching ureteric bud tips is an active area of interest (100, 101). Our simulations show some intriguing curvature of the ureteric bud local to sites of nephron condensation, suggesting that this may be more of a "chicken and egg" problem than previously recognized. The renal stroma, which forms "ribbons" that divide niches and surround newly forming nephrons, was recently shown to have significant spatial heterogeneity local to the niche and along the corticomedullary axis (102, 103), and basal adhesion of cells to surrounding stroma may contribute to sorting outcomes (44). The contribution of ureteric bud and stromal cells could be readily integrated in future work. Second, removing cells from their native tissue environment risks distorting readout of true in vivo biophysical properties by altering surface adhesion receptor integrity and limiting measurements to those possible through cell interactions with an appropriate traction force substrate or single partner cell type in adhesion measurements. For many questions, these caveats are likely to be a reasonable tradeoff against the volume of information that can be gathered by MATCHY compared to the few in vivo measurement tools that exist (38, 104–110). Third, we used a simplified model that neglected possible contributions of continuous cell differentiation and proliferation to early nephron morphology. Progressive recruitment of differentiating cells (85) and cell proliferation likely have a role in defining especially the spatial structure of nephron segments after initial nephron condensation. In preliminary data, we indeed found that adding a serial cell differentiation process to the model increased the fraction of early nephron structures scored as having a linear sorting state after they self-organized (*SI Appendix*, Fig. S4, Movie S1*B*, and *Methods*). The model can be readily modified to further accommodate these features in future work.

In summary, MATCHY contributes a high-throughput and user-friendly extension to existing cell biophysical characterization techniques. MATCHY provides a powerful benchmarking tool for mechanobiology studies and emerging tissue engineering strategies. These seek to synthetically control and leverage self-organization principles to build complex tissue "seeds" with further developmental potential (28, 41, 111). In the kidney engineering space, for example, such tight feedback between multicellular design, biophysical measurement, structure prediction, and in vitro reconstitution carries a promising potential to control nephron formation, polarization, and connectivity. Kidney tissues assembled by leveraging biophysical principles have enormous potential to contribute a third arm to kidney replacement strategies beyond transplantation and dialysis in the future.

Methods

Full methods are provided in *SI Appendix*. Distal nephron and ureteric bud epithelial cells were derived from GATA3^{YFP} and GATA3^{mCherry} transgenic reporter iPSC lines according to published protocols (112, 113). MDCK-hRET9 and MDCK-hRET9^{KM} cell lines (56) were cultured in a selection medium containing 100 μg mL^{-1} neomycin (G418, 50 μg mL^{-1} stock, Penn Cell Center) to remove nonexpressing cells. Mouse protocols followed NIH guidelines and were approved by the Institutional Animal Care and Use Committee of the University of Pennsylvania. Mouse embryonic kidneys were dissected from E17 embryos collected from timed pregnant CD-1 mice (Charles River) and stages confirmed by limb anatomy as previously described (114).

Primary cell dissociation was achieved through 0.5% pancreatin (Sigma-Aldrich, P7545) and 0.25% Collagenase A (Sigma-Aldrich, C0130) treatment. MATCHY microfabrication followed SU-8 photoresist on silicon wafer, polyacrylamide gelation, and surface treatment protocols. MATCHY traction force and cell–cell adhesion protocols are provided in *SI Appendix*. Cellular Potts modeling was implemented in Python. Gene expression matrices generated from scRNA-seq of dissociated E18.5 mouse embryonic kidneys in Combes et al. were used for feature plots and gene set enrichment analysis (82).

Data, Materials, and Software Availability. MATCHY code and agent-based modeling code are available at https://github.com/jiageng409/HughesLab_MATCHY_Pipeline (115). All experiment data necessary for the interpretation of results are included in the manuscript and supporting information.

ACKNOWLEDGMENTS. We are grateful to Gregory Dressler (University of Michigan) for the generous gift of MDCK-RET and MDCK-RET KM cells. We thank John Viola and Samuel Grindel for sharing their expertise on experiment protocols and spheroid segmentation. We thank Catherine Porter for contributing art to the MATCHY workflow schematic. This work was carried out in part at the Singh Center for Nanotechnology at the University of Pennsylvania supported by the NSF National Nanotechnology Coordinated Infrastructure Program (NNCI-2025608). This research was partially supported by the NSF through the University of Pennsylvania Materials Research Science and Engineering Center (MRSEC, DMR-2309043). This work was supported by an NSF GRFP award (J.L.), NIH F32 DK126385 (L.S.P.), NIH NIGMS MIRA R35GM133380 (A.J.H.), NIH NIDDK R01DK132296 (A.J.H.), and NSF CAREER award 2047271 (A.J.H.).

Author affiliations: [a]Department of Bioengineering, University of Pennsylvania, Philadelphia, PA 19104; [b]Bioengineering Graduate Group, University of Pennsylvania, Philadelphia, PA 19104; [c]Center for Soft and Living Matter, University of Pennsylvania, Philadelphia, PA 19104; [d]Department of Cell and Developmental Biology, University of Pennsylvania, Philadelphia, PA 19104; [e]Cell and Molecular Biology Graduate Group, University of Pennsylvania, Philadelphia, PA 19104; [f]Center for Precision Engineering for Health, University of Pennsylvania, Philadelphia, PA 19104; [g]Materials Research Science and Engineering Center, University of Pennsylvania, Philadelphia, PA 19104; and [h]Institute for Regenerative Medicine, University of Pennsylvania, Philadelphia, PA 19104

Author contributions: J.L. and A.J.H. designed research; J.L., L.S.P., and A.Z.H. performed research; J.L. contributed new reagents/analytic tools; J.L. and A.J.H. analyzed data; and J.L. and A.J.H. wrote the paper.

1. C.-P. Heisenberg, Y. Bellaïche, Forces in tissue morphogenesis and patterning. *Cell* **153**, 948–962 (2013).
2. S. Yang *et al.*, Morphogens enable interacting supracellular phases that generate organ architecture. *Science* **382**, eadg5579 (2023).
3. A. E. Shyer *et al.*, Emergent cellular self-organization and mechanosensation initiate follicle pattern in the avian skin. *Science* **357**, 811–815 (2017).
4. R. M. Houtekamer, M. C. van der Net, M. M. Maurice, M. Gloerich, Mechanical forces directing intestinal form and function. *Curr. Biol.* **32**, R791–R805 (2022).
5. C. Parada *et al.*, Mechanical feedback defines organizing centers to drive digit emergence. *Dev. Cell* **57**, 854–866.e6 (2022).
6. T. Mammoto *et al.*, Mechanochemical control of mesenchymal condensation and embryonic tooth organ formation. *Dev. Cell* **21**, 758–769 (2011).
7. M. H. Dominguez, A. L. Krup, J. M. Muncie, B. G. Bruneau, Graded mesoderm assembly governs cell fate and morphogenesis of the early mammalian heart. *Cell* **186**, 479–496.e23 (2023).
8. H. Tao *et al.*, Oscillatory cortical forces promote three dimensional cell intercalations that shape the murine mandibular arch. *Nat. Commun.* **10**, 1703 (2019).
9. V. Osathanondh, E. L. Potter, Development of human kidney as shown by microdissection. IV. Development of tubular portions of nephrons. *Arch. Pathol.* **82**, 391–402 (1966).
10. A. N. Combes, J. A. Davies, M. H. Little, Cell-cell interactions driving kidney morphogenesis. *Curr. Top. Dev. Biol.* **112**, 467–508 (2015).
11. T. J. Carroll, J.-S. Park, S. Hayashi, A. Majumdar, A. P. McMahon, Wnt9b plays a central role in the regulation of mesenchymal to epithelial transitions underlying organogenesis of the mammalian urogenital system. *Dev. Cell* **9**, 283–292 (2005).
12. J.-S. Park, M. T. Valerius, A. P. McMahon, Wnt/beta-catenin signaling regulates nephron induction during mouse kidney development. *Development* **134**, 2533–2539 (2007).
13. A. C. Brown *et al.*, Role for compartmentalization in nephron progenitor differentiation. *Proc. Natl. Acad. Sci. U.S.A.* **110**, 4640–4645 (2013).
14. A. Ihermann-Hella *et al.*, Dynamic MAPK/ERK activity sustains nephron progenitors through niche regulation and primes precursors for differentiation. *Stem Cell Rep.* **11**, 912–928 (2018).
15. N. O. Lindström, N. O. Carragher, P. Hohenstein, The PI3K pathway balances self-renewal and differentiation of nephron progenitor cells through β-catenin signaling. *Stem Cell Rep.* **4**, 551–560 (2015).
16. A. Reginensi *et al.*, Yap- and Cdc42-dependent nephrogenesis and morphogenesis during mouse kidney development. *PLoS Genet.* **9**, e1003380 (2013).
17. A. Das *et al.*, Stromal-epithelial crosstalk regulates kidney progenitor cell differentiation. *Nat. Cell Biol.* **15**, 1035–1044 (2013).
18. H. Wang *et al.*, STAT1 activation regulates proliferation and differentiation of renal progenitors. *Cell. Signal.* **22**, 1717–1726 (2010).
19. N. O. Lindström *et al.*, Integrated β-catenin, BMP, PTEN, and Notch signalling patterns the nephron. *Elife* **3**, e04000 (2015).
20. S. C. Boyle, M. Kim, M. T. Valerius, A. P. McMahon, R. Kopan, Notch pathway activation can replace the requirement for Wnt4 and Wnt9b in mesenchymal-to-epithelial transition of nephron stem cells. *Development* **138**, 4245–4254 (2011).
21. E. Chung, P. Deacon, S. Marable, J. Shin, J.-S. Park, Notch signaling promotes nephrogenesis by downregulating Six2. *Development* **143**, 3907–3913 (2016).
22. J. G. Lefevre *et al.*, Self-organisation after embryonic kidney dissociation is driven via selective adhesion of ureteric epithelial cells. *Development* **144**, 1087–1096 (2017).
23. E. A. Cho *et al.*, Differential expression and function of cadherin-6 during renal epithelium development. *Development* **125**, 803–812 (1998).
24. S. P. Mah, H. Saueressig, M. Goulding, C. Kintner, G. R. Dressler, Kidney development in cadherin-6 mutants: Delayed mesenchyme-to-epithelial conversion and loss of nephrons. *Dev. Biol.* **223**, 38–53 (2000).
25. S. Goto *et al.*, Involvement of R-cadherin in the early stage of glomerulogenesis. *J. Am. Soc. Nephrol.* **9**, 1234–1241 (1998).
26. H. Y. Kim, T. R. Jackson, L. A. Davidson, On the role of mechanics in driving mesenchymal-to-epithelial transitions. *Semin. Cell Dev. Biol.* **67**, 113–122 (2017).
27. A. Sharma *et al.*, FGF8 induces chemokinesis and regulates condensation of mouse nephron progenitor cells. *Development* **149**, dev201012 (2022).
28. A. Gupta, M. P. Lutolf, A. J. Hughes, K. F. Sonnen, Bioengineering in vitro models of embryonic development. *Stem Cell Rep.* **16**, 1104–1116 (2021).
29. G. Binnig, C. F. Quate, C. Gerber, Atomic force microscope. *Phys. Rev. Lett.* **56**, 930–933 (1986).
30. H.-J. Butt, B. Cappella, M. Kappl, Force measurements with the atomic force microscope: Technique, interpretation and applications. *Surf. Sci. Rep.* **59**, 1–152 (2005).
31. B. A. Nerger *et al.*, 3D hydrogel encapsulation regulates nephrogenesis in kidney organoids. *Adv. Mater.* **36**, e2308325 (2024).
32. R. M. Hochmuth, Micropipette aspiration of living cells. *J. Biomech.* **33**, 15–22 (2000).
33. B. Hogan, A. Babataheri, Y. Hwang, A. I. Barakat, J. Husson, Characterizing cell adhesion by using micropipette aspiration. *Biophys. J.* **109**, 209–219 (2015).
34. T. Y.-C. Tsai *et al.*, An adhesion code ensures robust pattern formation during tissue morphogenesis. *Science* **370**, 113–116 (2020).
35. H. Zhang, K.-K. Liu, Optical tweezers for single cells. *J. R. Soc. Interface* **5**, 671–690 (2008).
36. L. Novotny, R. X. Bian, X. S. Xie, Theory of nanometric optical tweezers. *Phys. Rev. Lett.* **79**, 645–648 (1997).
37. D. Molino *et al.*, On-chip quantitative measurement of mechanical stresses during cell migration with emulsion droplets. *Sci. Rep.* **6**, 29113 (2016).
38. F. Serwane *et al.*, In vivo quantification of spatially varying mechanical properties in developing tissues. *Nat. Methods* **14**, 181–186 (2017).
39. M. Dembo, Y.-L. Wang, Stresses at the cell-to-substrate interface during locomotion of fibroblasts. *Biophys. J.* **76**, 2307–2316 (1999).
40. B. Sabass, M. L. Gardel, C. M. Waterman, U. S. Schwarz, High resolution traction force microscopy based on experimental and computational advances. *Biophys. J.* **94**, 207–220 (2008).
41. M. Bao *et al.*, Stem cell-derived synthetic embryos self-assemble by exploiting cadherin codes and cortical tension. *Nat. Cell Biol.* **24**, 1341–1349 (2022).
42. M. Lusis *et al.*, Isolation of clonogenic, long-term self renewing embryonic renal stem cells. *Stem Cell Res.* **5**, 23–39 (2010).
43. C. Xinaris *et al.*, In vivo maturation of functional renal organoids formed from embryonic cell suspensions. *J. Am. Soc. Nephrol.* **23**, 1857–1868 (2012).
44. A. E. Cerchiari *et al.*, A strategy for tissue self-organization that is robust to cellular heterogeneity and plasticity. *Proc. Natl. Acad. Sci. U.S.A.* **112**, 2287–2292 (2015).
45. M. C. Recuenco *et al.*, Nonmuscle myosin II regulates the morphogenesis of metanephric mesenchyme-derived immature nephrons. *J. Am. Soc. Nephrol.* **26**, 1081–1091 (2015).
46. U. Muller *et al.*, Integrin α8β1 is critically important for epithelial-mesenchymal interactions during kidney morphogenesis. *Cell* **88**, 603–613 (1997).
47. K. Leclerc, F. Costantini, Mosaic analysis of cell rearrangements during ureteric bud branching in dissociated/reaggregated kidney cultures and in vivo. *Dev. Dyn.* **245**, 483–496 (2016).
48. M. Unbekandt, J. A. Davies, Dissociation of embryonic kidneys followed by reaggregation allows the formation of renal tissues. *Kidney Int.* **77**, 407–416 (2010).
49. V. Ganeva, M. Unbekandt, J. A. Davies, An improved kidney dissociation and reaggregation culture system results in nephrons arranged organotypically around a single collecting duct system. *Organogenesis* **7**, 83–87 (2011).
50. B. Der, H. Bugacov, B.-M. Briantseva, A. P. McMahon, Cadherin adhesion complexes direct cell aggregation in the epithelial transition of Wnt-induced nephron progenitor cells. bioRxiv [Preprint] (2023). https://doi.org/10.1101/2023.08.27.555021. Accessed 02 September 2024.
51. U. Dahl *et al.*, Genetic dissection of cadherin function during nephrogenesis. *Mol. Cell. Biol.* **22**, 1474–1487 (2002).
52. T. Y.-C. Tsai, R. M. Garner, S. G. Megason, Adhesion-based self-organization in tissue patterning. *Annu. Rev. Cell Dev. Biol.* **38**, 349–374 (2022).
53. M. S. Steinberg, Reconstruction of tissues by dissociated cells. *Science* **141**, 401–408 (1963).
54. G. W. Brodland, The differential interfacial tension hypothesis (DITH): A comprehensive theory for the self-rearrangement of embryonic cells and tissues. *J. Biomech. Eng.* **124**, 188–197 (2002).
55. L. Saxen, J. Wartiovaara, Cell contact and cell adhesion during tissue organization. *Int. J. Cancer* **1**, 271–290 (1966).
56. M. J. Tang, D. Worley, M. Sanicola, G. R. Dressler, The RET-glial cell-derived neurotrophic factor (GDNF) pathway stimulates migration and chemoattraction of epithelial cells. *J. Cell Biol.* **142**, 1337–1345 (1998).
57. C. E. Fisher, L. Michael, M. W. Barnett, J. A. Davies, Erk MAP kinase regulates branching morphogenesis in the developing mouse kidney. *Development* **128**, 4329–4338 (2001).
58. K. Kurtzeborn *et al.*, Biomechanical regulation of cell shapes promotes branching morphogenesis of the ureteric bud epithelium. bioRxiv [Preprint] (2024). https://doi.org/10.1101/2024.03.28.585666. Accessed 02 September 2024.

59. A. Schuchardt, V. D'Agati, L. Larsson-Blomberg, F. Costantini, V. Pachnis, Defects in the kidney and enteric nervous system of mice lacking the tyrosine kinase receptor Ret. *Nature* **367**, 380–383 (1994).
60. J. G. Pichel *et al.*, Defects in enteric innervation and kidney development in mice lacking GDNF. *Nature* **382**, 73–76 (1996).
61. N. Hino *et al.*, ERK-mediated mechanochemical waves direct collective cell polarization. *Dev. Cell* **53**, 646–660.e8 (2020).
62. J. N. Lakins, A. R. Chin, V. M. Weaver, Exploring the link between human embryonic stem cell organization and fate using tension-calibrated extracellular matrix functionalized polyacrylamide gels. *Methods Mol. Biol.* **916**, 317–350 (2012).
63. L. S. Prahl, C. M. Porter, J. Liu, J. M. Viola, A. J. Hughes, Independent control over cell patterning and adhesion on hydrogel substrates for tissue interface mechanobiology. *iScience* **26**, 106657 (2023).
64. A. J. Hughes *et al.*, Single-cell western blotting. *Nat. Methods* **11**, 749–755 (2014).
65. J.-L. Maître, R. Niwayama, H. Turlier, F. Nédélec, T. Hiiragi, Pulsatile cell-autonomous contractility drives compaction in the mouse embryo. *Nat. Cell Biol.* **17**, 849–855 (2015).
66. T. Vignaud *et al.*, Stress fibres are embedded in a contractile cortical network. *Nat. Mater.* **20**, 410–420 (2021).
67. Q. Tseng *et al.*, Spatial organization of the extracellular matrix regulates cell–cell junction positioning. *Proc. Natl. Acad. Sci. U.S.A.* **109**, 1506–1511 (2012).
68. J. M. Viola *et al.*, Rho/ROCK activity tunes cell compartment segregation and differentiation in nephron-forming niches. bioRxiv [Preprint] (2023). https://doi.org/10.1101/2023.11.08.566308. Accessed 02 September 2024.
69. G. Cacalano *et al.*, GFRa1 is an essential receptor component for GDNF in the developing nervous system and kidney. *Neuron* **21**, 53–62 (1998).
70. L. Michael, D. E. Sweeney, J. A. Davies, A role for microfilament-based contraction in branching morphogenesis of the ureteric bud. *Kidney Int.* **68**, 2010–2018 (2005).
71. M. V. Barone *et al.*, RET/PTC1 oncogene signaling in PC Cl 3 thyroid cells requires the small GTP-binding protein Rho. *Oncogene* **20**, 6973–6982 (2001).
72. L. Saxén, H. Sariola, Early organogenesis of the kidney. *Pediatr. Nephrol.* **1**, 385–392 (1987).
73. K. M. Short *et al.*, Global quantification of tissue dynamics in the developing mouse kidney. *Dev. Cell* **29**, 188–202 (2014).
74. V. Osathanondh, E. L. Potter, Development of human kidney as shown by microdissection. III. Formation and interrelationship of collecting tubules and nephrons. *Arch. Pathol.* **76**, 290–302 (1963).
75. K. Stark, S. Vainio, G. Vassileva, A. P. McMahon, Epithelial transformation of metanephric mesenchyme in the developing kidney regulated by Wnt-4. *Nature* **372**, 679–683 (1994).
76. L. Canty, E. Zarour, L. Kashkooli, P. François, F. Fagotto, Sorting at embryonic boundaries requires high heterotypic interfacial tension. *Nat. Commun.* **8**, 157 (2017).
77. M. L. Manning, R. A. Foty, M. S. Steinberg, E.-M. Schoetz, Coaction of intercellular adhesion and cortical tension specifies tissue surface tension. *Proc. Natl. Acad. Sci. U.S.A.* **107**, 12517–12522 (2010).
78. G. Klein, M. Langegger, C. Goridis, P. Ekblom, Neural cell adhesion molecules during embryonic induction and development of the kidney. *Development* **102**, 749–761 (1988).
79. Y. Kimura *et al.*, Cadherin-11 expressed in association with mesenchymal morphogenesis in the head, somite, and limb bud of early mouse embryos. *Dev. Biol.* **169**, 347–358 (1995).
80. D. Vestweber, R. Kemler, P. Ekblom, Cell-adhesion molecule uvomorulin during kidney development. *Dev. Biol.* **112**, 213–221 (1985).
81. J. A. Davies, D. R. Garrod, Induction of early stages of kidney tubule differentiation by lithium ions. *Dev. Biol.* **167**, 50–60 (1995).
82. A. N. Combes *et al.*, Single cell analysis of the developing mouse kidney provides deeper insight into marker gene expression and ligand-receptor crosstalk. *Development* **146**, dev178673 (2019).
83. K. Kretzschmar, F. M. Watt, Lineage tracing. *Cell* **148**, 33–45 (2012).
84. K. Georgas *et al.*, Analysis of early nephron patterning reveals a role for distal RV proliferation in fusion to the ureteric tip via a cap mesenchyme-derived connecting segment. *Dev. Biol.* **332**, 273–286 (2009).
85. N. O. Lindström *et al.*, Progressive recruitment of mesenchymal progenitors reveals a time-dependent process of cell fate acquisition in mouse and human nephrogenesis. *Dev. Cell* **45**, 651–660.e4 (2018).
86. N. O. Lindström *et al.*, Spatial transcriptional mapping of the human nephrogenic program. *Dev. Cell* **56**, 2381–2398.e6 (2021).
87. P. Tikka *et al.*, Computational modelling of nephron progenitor cell movement and aggregation during kidney organogenesis. *Math. Biosci.* **344**, 108759 (2022).
88. A. N. Combes, J. G. Lefevre, S. Wilson, N. A. Hamilton, M. H. Little, Cap mesenchyme cell swarming during kidney development is influenced by attraction, repulsion, and adhesion to the ureteric tip. *Dev. Biol.* **418**, 297–306 (2016).
89. L. L. O'Brien *et al.*, Wnt11 directs nephron progenitor polarity and motile behavior ultimately determining nephron endowment. *Elife* **7**, e40392 (2018).
90. J. W. Mugford, J. Yu, A. Kobayashi, A. P. McMahon, High-resolution gene expression analysis of the developing mouse kidney defines novel cellular compartments within the nephron progenitor population. *Dev. Biol.* **333**, 312–323 (2009).
91. C. Wei, M. Larsen, M. P. Hoffman, K. M. Yamada, Self-organization and branching morphogenesis of primary salivary epithelial cells. *Tissue Eng.* **13**, 721–735 (2007).
92. M. Romeih, I. Cakstina, M. H. Zile, Retinoic acid is a negative physiological regulator of N-cadherin during early avian heart morphogenesis. *Dev. Growth Differ.* **51**, 753–767 (2009).
93. D. Duguay, R. A. Foty, M. S. Steinberg, Cadherin-mediated cell adhesion and tissue segregation: Qualitative and quantitative determinants. *Dev. Biol.* **253**, 309–323 (2003).
94. H.-G. Kang *et al.*, E-cadherin cell-cell adhesion in ewing tumor cells mediates suppression of anoikis through activation of the ErbB4 tyrosine kinase. *Cancer Res.* **67**, 3094–3105 (2007).
95. N. Naiman *et al.*, Repression of interstitial identity in nephron progenitor cells by Pax2 establishes the nephron-interstitium boundary during kidney development. *Dev. Cell* **41**, 349–365.e3 (2017).
96. C. M. Karner *et al.*, Wnt9b signaling regulates planar cell polarity and kidney tubule morphogenesis. *Nat. Genet.* **41**, 793–799 (2009).
97. M. H. Little, A. N. Combes, Kidney organoids: Accurate models or fortunate accidents. *Genes Dev.* **33**, 1319–1345 (2019).
98. R. Kopan, H.-T. Cheng, K. Surendran, Molecular insights into segmentation along the proximal-distal axis of the nephron. *J. Am. Soc. Nephrol.* **18**, 2014–2020 (2007).
99. C. R. Pfeifer, A. E. Shyer, A. R. Rodrigues, Creative processes during vertebrate organ morphogenesis: Biophysical self-organization at the supracellular scale. *Curr. Opin. Cell Biol.* **86**, 102305 (2024).
100. M. Mederacke, L. Conrad, N. Doumpas, R. Vetter, D. Iber, Geometric effects position renal vesicles during kidney development. *Cell Rep.* **42**, 113526 (2023).
101. H. Ramalingam *et al.*, Disparate levels of beta-catenin activity determine nephron progenitor cell fate. *Dev. Biol.* **440**, 13–21 (2018).
102. A. R. England *et al.*, Identification and characterization of cellular heterogeneity within the developing renal interstitium. *Development* **147**, dev190108 (2020).
103. S. B. Wilson, M. H. Little, The origin and role of the renal stroma. *Development* **148**, dev199886 (2021).
104. O. Campàs, A toolbox to explore the mechanics of living embryonic tissues. *Semin. Cell Dev. Biol.* **55**, 119–130 (2016).
105. N. Yamaguchi *et al.*, Rear traction forces drive adherent tissue migration in vivo. *Nat. Cell Biol.* **24**, 194–204 (2022).
106. A. Mongera *et al.*, A fluid-to-solid jamming transition underlies vertebrate body axis elongation. *Nature* **561**, 401–405 (2018).
107. J. M. Viola *et al.*, Tubule jamming in the developing mouse kidney creates cyclical mechanical stresses in nephron-forming niches. bioRxiv [Preprint] (2023). https://doi.org/10.1101/2022.06.03.494718. Accessed 02 September 2024.
108. G. Scarcelli *et al.*, Noncontact three-dimensional mapping of intracellular hydromechanical properties by Brillouin microscopy. *Nat. Methods* **12**, 1132–1134 (2015).
109. J. Zhang, G. Scarcelli, Mapping mechanical properties of biological materials via an add-on Brillouin module to confocal microscopes. *Nat. Protoc.* **16**, 1251–1275 (2021).
110. K. Sugimura, P.-F. Lenne, F. Graner, Measuring forces and stresses in situ in living tissues. *Development* **143**, 186–196 (2016).
111. A. C. Daly, M. E. Prendergast, A. J. Hughes, J. A. Burdick, Bioprinting for the Biologist. *Cell* **184**, 18–32 (2021).
112. S. E. Howden *et al.*, Plasticity of distal nephron epithelia from human kidney organoids enables the induction of ureteric tip and stalk. *Cell Stem Cell* **28**, 671–684.e6 (2021).
113. S. V. Kumar *et al.*, Kidney micro-organoids in suspension culture as a scalable source of human pluripotent stem cell-derived kidney cells. *Development* **146**, dev172361 (2019).
114. N. Wanek, K. Muneoka, G. Holler-Dinsmore, R. Burton, S. V. Bryant, A staging system for mouse limb development. *J. Exp. Zool.* **249**, 41–49 (1989).
115. J. Liu, L.S. Prahl, A. Huang, A.J. Hughes, HughesLab_MATCHY_Pipeline. GitHub. https://github.com/jiageng409/HughesLab_MATCHY_Pipeline. Deposited 30 Jun 2024.